Monthly Notices
of the
ROYAL ASTRONOMICAL SOCIETY

MNRAS **494,** 2221–2235 (2020)
Advance Access publication 2020 March 9

doi:10.1093/mnras/staa640

Understanding nebular spectra of Type Ia supernovae

Kevin D. Wilk,[1]★ D. John Hillier[1] and Luc Dessart[2]

[1]*Department of Physics and Astronomy, Pittsburgh Particle Physics, Astrophysics, and Cosmology Center (PITT PACC), University of Pittsburgh, Pittsburgh, PA 15260, USA,*
[2]*Departamento de Astronomía, Universidad de Chile, Unidad Mixta Internacional Franco-Chilena de Astronomía (CNRS UMI 3386), Camino El Observatorio 1515, Las Condes, 7550000 Santiago, Chile*

Accepted 2020 February 24. Received 2020 February 23; in original form 2019 July 8

ABSTRACT

In this study, we present one-dimensional, non-local-thermodynamic-equilibrium, radiative transfer simulations (using CMFGEN) in which we introduce micro-clumping at nebular times into two Type Ia supernova ejecta models. We use one sub-Chandrasekhar (sub-$M_{\rm Ch}$) ejecta model with 1.04 $M_\odot$ and one Chandrasekhar ($M_{\rm Ch}$) ejecta model with 1.40 $M_\odot$. We introduce clumping factors $f = 0.33$, 0.25, and 0.10, which are constant throughout the ejecta, and compare results to the unclumped $f = 1.0$ case. We find that clumping is a natural mechanism to reduce the ionization of the ejecta, reducing emission from [Fe III], [Ar III], and [S III] by a factor of a few. For decreasing values of the clumping factor f, the [Ca II] $\lambda\lambda$7291,7324 doublet became a dominant cooling line for our $M_{\rm Ch}$ model but remained weak in our sub-$M_{\rm Ch}$ model. Strong [Ca II] $\lambda\lambda$7291,7324 indicates non-thermal heating in that region and may constrain explosion modelling. Due to the low abundance of stable nickel, our sub-$M_{\rm Ch}$ model never showed the [Ni II] 1.939-μm diagnostic feature for all clumping values.

Key words: radiative transfer – supernovae: general – white dwarfs.

1 INTRODUCTION

The general consensus is that Type Ia supernovae (SNe Ia) are thermonuclear explosions of carbon–oxygen (C/O) white dwarfs (WDs; Hoyle & Fowler 1960). Whether this explosion arises in a system with one WD and a non-degenerate star [known as the single degenerate (SD) channel] or in a system with two WDs [known as the double degenerate (DD) channel] remains uncertain.

SNe Ia come from compact WDs and cool quickly via adiabatic expansion, and without an additional energy supply, they would be extremely difficult to detect. What powers the observed luminosity of SNe Ia is the decay of radioactive material produced during the explosion. The main radioactive isotope produced is ^{56}Ni, whose decay chain is ^{56}Ni→^{56}Co→^{56}Fe, releasing 1.72 and 3.75 MeV for each part of the decay chain. Therefore, the production of ^{56}Ni is important in powering the luminosity of SNe Ia. However, the nickel yields (both stable and unstable) in SNe Ia are sensitive to both progenitor mass ($\rho_{\rm c}$) and explosion scenario.

In one-dimensional (1D) explosion modelling, higher central densities lead to enhanced electron capture and thus a larger neutron excess during the explosion. As a consequence, more stable nickel (^{58}Ni, ^{60}Ni, and ^{62}Ni) is produced (Nomoto 1984; Khokhlov 1991a, b). Sub-$M_{\rm Ch}$ WDs have lower central densities, and 1D modelling of SNe Ia from sub-$M_{\rm Ch}$ progenitors shows a lower abundance of ^{58}Ni and ^{60}Ni compared to $M_{\rm Ch}$ SNe Ia. However, three-dimensional (3D) DDT modelling does not produce a ^{56}Ni hole. Instead, the abundance of both ^{56}Ni and ^{58}Ni extends from the lowest velocities to about 10 000 km s^{-1} (Kasen, Röpke & Woosley 2009; Seitenzahl et al. 2013). This result arises because ignition occurs in the centre of the WD. If ignition occurs on the surface, as in a double detonation, the burning front moves in and there is no mixing outwards of what little stable Ni is produced (Woosley & Weaver 1994; Livne & Arnett 1995; Fink, Hillebrandt & Röpke 2007; Fink et al. 2010). Overall, the 3D simulations of WD explosions remain somewhat artificial, and the outcome depends strongly on the number of ignition points and their distribution. Despite the time-scale for gravitational settling being $\sim$10^9–10^{10} yr (Bildsten & Hall 2001), ^{22}Ne settling in sub-$M_{\rm Ch}$ is proposed as a way to enhance the neutronization. Therefore, nebular spectral features of nickel and other iron-group elements (IGEs) may constrain the physics of SNe Ia (Woosley 1997; Iwamoto et al. 1999; Stehle et al. 2005; Mazzali & Podsiadlowski 2006; Gerardy et al. 2007; Maeda et al. 2010a; Mazzali et al. 2011, 2015; Mazzali & Hachinger 2012).

Without knowing the progenitor system and explosion scenario, we cannot accurately predict the amount of stable nickel produced, the overall abundances of intermediate-mass elements (IMEs), and where in the ejecta these IMEs are produced relative to the ^{56}Ni. However, studying nebular spectra will allow us to estimate these properties. At nebular times, any nickel emission features are due to the remaining stable nickel, particularly from ^{58}Ni and ^{60}Ni. Since

★ E-mail: kdw25@pitt.edu

Table 1. Model mass information in $M_\odot$ at 0.75 d post-explosion. The parentheses (#) correspond to $\times 10^{\#}$.

Model	Mass ($M_\odot$)	S ($M_\odot$)	Ar ($M_\odot$)	Ca ($M_\odot$)	Fe ($M_\odot$)	Co ($M_\odot$)	^{58}Ni + ^{60}Ni ($M_\odot$)	^{56}Ni ($M_\odot$)
SUB1	1.04	1.046(−1)	2.273(−2)	2.361(−2)	2.226(−2)	5.526(−2)	1.113(−2)	5.684(−1)
CHAN	1.40	1.661(−1)	3.693(−2)	4.120(−2)	1.020(−1)	5.713(−2)	2.517(−2)	5.708(−1)

the width of any observed nebular feature is influenced by emission over the velocities at which the species exist, stable nickel features may help constrain the presence of the ^{56}Ni hole (irrespective of the model).

Nebular spectra are great tools to understand progenitors of SNe Ia. At this time, the ejecta is optically thin in the continuum and in most lines [with exceptions such as ultraviolet (UV) transitions], and much of the spectra comes from the inner part of the ejecta ($\lesssim$8000 km s^{-1}), where the densities are highest and iron is the most abundant species. Because iron is most abundant in this region at nebular times, optical spectra are dominated by Fe II and Fe III lines and exhibit little to no flux from IME species such as S III and Ar III. The [Ca II] λλ7291, 7324 doublet may be blended with the [Fe II] λλ7155, 7172, 7388 triplet, so its presence is difficult to determine.

Numerous previous studies have investigated SN Ia nebular spectra (Houck & Fransson 1992; Ruiz-Lapuente, Lucy & Danziger 1992; Ruiz-Lapuente et al. 1995; Smareglia & Mazzali 1997; Mazzali et al. 1998; Gerardy 2002; Kozma et al. 2005; Maeda et al. 2010b; Blondin et al. 2012; Taubenberger et al. 2013b; Dong et al. 2015; Mazzali et al. 2015; Black, Fesen & Parrent 2016; Botyánszki & Kasen 2017; Graham et al. 2017; Black 2018; Diamond et al. 2018; Maguire et al. 2018; Black, Fesen & Parrent 2019). Authors often study emission lines by fitting Gaussian profiles to features, which may or may not be blended. Maguire et al. (2018), for instance, fit Gaussian profiles to emission lines, and assumed the levels were in local thermodynamic equilibrium (LTE) with respect to the ground state. These authors also try and fit the complicated feature around 7300 Å without knowing the possible contribution from [Ca II] λλ7291, 7324. Taubenberger et al. (2013b) utilized nebular spectra to understand the emission from [O I] λλ6300, 6364 in the sub-luminous SN2010lp (SN1991bg-like). These authors argued for a non-spherical distribution of oxygen located close to the core to produce these features.

Ruiz-Lapuente et al. (1995) struggled to obtain good model fits to nebular spectra despite their models matching the photospheric phase spectra. These authors also note the dominant form of iron is Fe^{2+}, with a sizeable fraction of Fe^{+} that need not be coincident with Fe^{2+}. Ruiz-Lapuente et al. (1992) modelled spectra for distance determination by solving for the ionization structure, assuming collisional excitations dominate, and the energy loss is balanced by the thermalization of γ-rays and positrons from nuclear decays. These authors were able to fit some features (like the [Fe III] 4700-Å blend) to nebular spectra.

Mazzali et al. (2015) have also obtained nebular spectral fits to SN2011fe with their 'ρ-11fe' model by means of abundance tomography. The authors claim that SN2011fe requires the innermost ejecta to be dominated by stable iron, which aids in cooling instead of heating (via radioactive decay) and rules out a low-mass ($\sim$1.04 $M_\odot$) WD progenitor. However, as shown later, the ionization is sensitive to the amount of clumping. In addition, since the abundances of Fe^{+} and Fe^{2+} are (or may be) comparable, the relative strength of [Fe II] and [Fe III] will be affected by errors in the atomic data. In contrast to Mazzali et al. (2015), our modelling favours a sub-Chandrasekhar WD for the progenitor of 2011fe.

Mazzali et al. (2018) also used abundance tomography to model the fast declining SNe Ia, SN2007on, and SN2011iv. By analysing emission components of many [Fe II] and [Fe III] features, the authors reproduce the spectra by using a two-component emission model (one blueshifted and one redshifted), which acts like two distinct nebulae. The authors do not rule out the possibility of an off-centre ignition instead of two colliding WDs. In all of these works, however, the abundances and their distributions are free parameters. Dong et al. (2015) also examine nebular spectra that show doubly peaked line profiles shifted by $\sim$5000 km s^{-1}. Dong et al. (2015) claim this to be the result of colliding WDs.

Nebular modelling raises questions about the ionization/abundance structure of 'normal' SN Ia ejecta. Nebular modelling by Botyánszki & Kasen (2017) and Wilk, Hillier & Dessart (2018) predicts strong emission lines of [S III] λλ9069, 9531 [and [Ar III] λ71336, 7751 by Wilk et al. (2018)] in their ejecta mass models. Why are these emission lines largely absent or weak in observations? What is the contribution of [Ca II] λλ7291, 7324 to the observed 7300 Å feature? What does it imply if IMEs are not seen in nebular spectra? Does this reflect the ionization structure or the abundances and/or chemical stratification? What causes the strength of the [Fe III] 4700 Å feature to be much stronger than other features beyond 5500 Å in models compared to observations (Botyánszki & Kasen 2017; Wilk et al. 2018)?

The nebular model spectra of Wilk et al. (2018) indicate a higher ionization than what is generally observed. As clumping enhances the density, increases the recombination rate, and lowers the ionization, we introduce clumping in our nebular modelling of SNe Ia ejecta. Given the high ionization of model SUB1 (a sub-$M_{\rm Ch}$ detonation ejecta model from Wilk et al. 2018; also see Section 2) at nebular times (because the lack of a '^{56}Ni hole' facilitates more heating of the inner region), clumping is a natural choice, given previous evidence of its role in reproducing spectral features (Chugai 1992; Bowers et al. 1997; Thomas et al. 2002; Leonard et al. 2005; Leloudas et al. 2009; Porter et al. 2016; Srivastav et al. 2016). Previous theoretical modelling suggests clumping to be a by-product of 'nickel bubbles', an expansion of the iron and nickel regions relative to the surrounding material due to radioactive decay energy deposition (Woosley 1988; Li, McCray & Sunyaev 1993; Basko 1994; Wang 2008), Rayleigh–Taylor instabilities during DDT burning (Golombek & Niemeyer 2005), or material interaction during detonation (Maier & Niemeyer 2006).

In this paper, we study the formation of nebular spectra and examine the influence of clumping. We highlight problems with the emission from IMEs and the ionization structure by examining the influence of clumping. In this study, we use models SUB1 and CHAN from Wilk et al. (2018). In Section 2, we discuss our technique for introducing clumping in our models. In Section 3 , we present the impact of clumping on nebular SN Ia spectra. We highlight the changes to the ionization structure in Section 3.2. Shifts in ionization are reflected in some species, so in Sections 3.3–3.5,

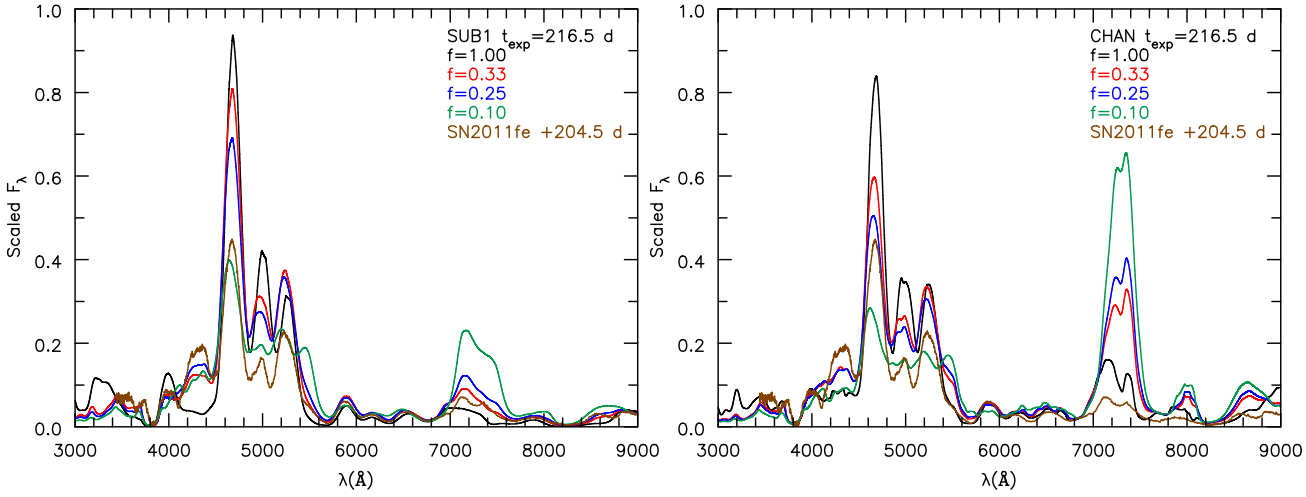

Figure 1. Comparison of SUB1 and CHAN models to SN2011fe. Flux values for SN2011fe have been scaled by 4.225×10^7 to account for models at 1 kpc. Then, all flux values were scaled by the same value that is of order unity. Data from SN2011fe are shown in brown and are 204.5 d post *B*-band maximum. The two most striking discrepancies between the models and observations are as follows: (i) the [Fe III] lines are too strong relative to the [Fe II] lines (especially in the unclumped models), and (ii) the overprediction of the [Ca II] doublet near 7300 Å (especially in model CHAN). The data were taken from the CfA Supernova Archive and collected from Yaron & Gal-Yam (2012) and Mazzali et al. (2015).

we discuss the effects on iron features, nickel features, and IMEs, respectively. Finally, we summarize our work in Section 4.

2 TECHNIQUE

2.1 Ejecta models

This research uses two hydrodynamic models of Wilk et al. (2018), DDC10 (CHAN) and SCH5p5 (SUB1). DDC10 is a $M_{\rm Ch}$ (1.40 $M_\odot$) model from Blondin et al. (2013). Model SCH5p5 is a sub-$M_{\rm Ch}$ (1.04 $M_\odot$) from Blondin et al. (2017), but we have scaled the density by 0.98 (see Wilk et al. 2018) in order to have the same ^{56}Ni. Both CHAN and SUB1 have the same ^{56}Ni at 0.62 $M_\odot$. However, CHAN has a stable iron core, whereas SUB1 does not. We use CMFGEN to solve the spherically symmetric, time-dependent, relativistic radiative transfer equation allowing for non-LTE processes. We take these two models at 216.5 d post-explosion from Wilk et al. (2018). Table 1 lists the initial masses for each model as well as the mass abundance of calcium, iron, cobalt, ^{58}Ni plus ^{60}Ni, and ^{56}Ni. We see CHAN has more than twice the amount of stable nickel – $M(^{58}\mathrm{Ni}) + M(^{60}\mathrm{Ni})$ – than SUB1 as well as almost a factor of 2 more calcium.

2.2 Numerical treatment

Our original radiative-transfer calculations for our models did not include the effects of clumping. Therefore, to treat clumping in our models, we make some simple assumptions with CMFGEN. We assume that the clumps are 'small' (i.e. smaller than a mean-free path) and occupy a fraction, *f*, of the total volume. *f* is known as the volume-filling factor, and can be defined as $f = \langle\rho\rangle^2/\langle\rho^2\rangle$, where ρ is the density. Throughout this paper, we use the term clumping factor synonymously with volume-filling factor.

We assume there is no interclump media and the clumping is uniform in a homogeneous flow [i.e. $f(V) = f_\circ$ for all species and velocities *V*]. Assumptions underlying our clumping approach and discussions of the influence of clumping on core-collapse SNe II-P are provided by Dessart, Hillier & Wilk (2018). Our treatment of clumping in CMFGEN differs from that of a concentric shell-type structure, which is susceptible to radiative-transfer effects across a shell and requires a large number of depth points to resolve the shells.

The clumping factor scales many variables, such as densities (scaled by 1/*f*) and the emissivities and opacities (calculated using the populations in the clumps and then scaled by *f*). This micro-clumping formalism leaves the mass column density unchanged. CMFGEN has incorporated this clumping method since Hillier & Miller (1999) first applied it to massive stars.

At a time-step of 216.5 d post-explosion (∼ + 200 d post-maximum), we re-solved the relativistic radiative-transfer equation for our models SUB1 and CHAN using a clumping factor (*f*) of 0.33, 0.25, and 0.10 (values partially motivated by modelling of radiation-driven winds in massive stars; see, e.g. Hillier & Miller 1999; Najarro 2001; Bouret et al. 2003; Puls et al. 2003). This range of values is also consistent with what has been inferred for clumps in planetary nebulae (Boffi & Stanghellini 1994; Stasińska et al. 2004; Ruiz et al. 2011). Since the previous time-step was not computed using clumping in the models, we scaled the initial input populations by 1/*f* between successive ionizations. This simple scaling is adequate since time-dependent effects have a negligible influence on the spectrum.

3 RESULTS

To highlight the drop in ionization due to clumping for normal-type SNe Ia, the optical spectrum of SN2011fe is plotted against the synthetic spectra of models SUB1 and CHAN for clumping values $f = 1.00$, 0.33, 0.25, and 0.10 in Fig. 1. For non-clumped models, [Fe III] lines are too strong while [Fe II] lines are too weak. As the clumping factor is increased, the [Fe III] lines weaken while [Fe II] lines strengthen. At the same time, the emission in the [Ca II] λλ7291, 7324 doublet increases. Comparison of the [Ca II] emission with that in SN2011fe shows that a much better fit is obtained with the sub-Chandrasekhar model.

Figs 2 and 3 show the synthetic optical and near-infrared (NIR) spectra of SUB1 and CHAN for the different values of a clumping

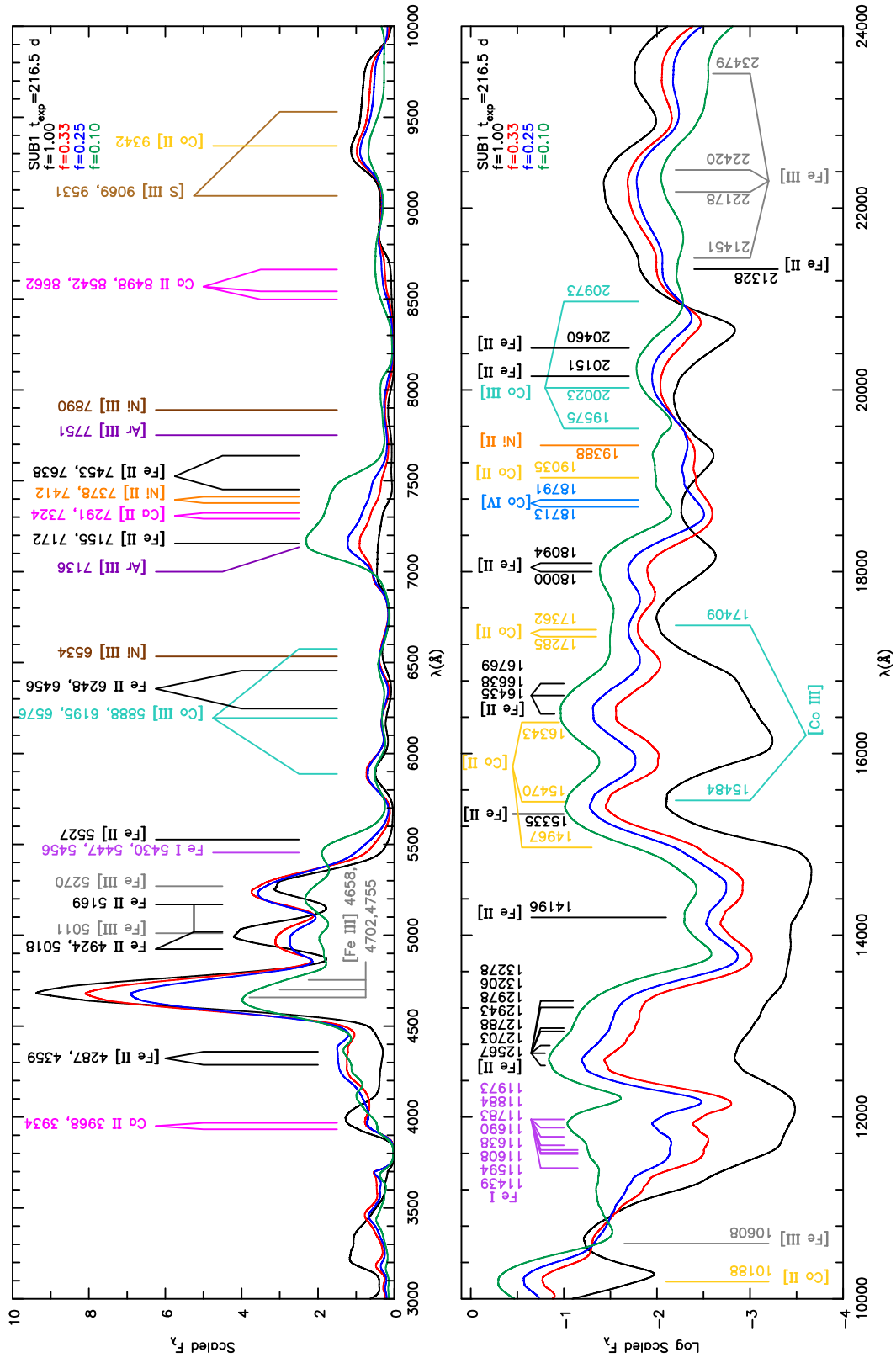

Figure 2. Spectra of SUB1 at 216.5 d post-explosion compared to the spectra computed using different clumping factor values (0.33, 0.25, and 0.10). The spectra have all been scaled by the same value. To contrast the little flux in the IR, we show the logarithm of the flux. In the IR, particularly from 10 000 to 11 800 Å, changes are several orders of magnitude for a factor of a few in density.

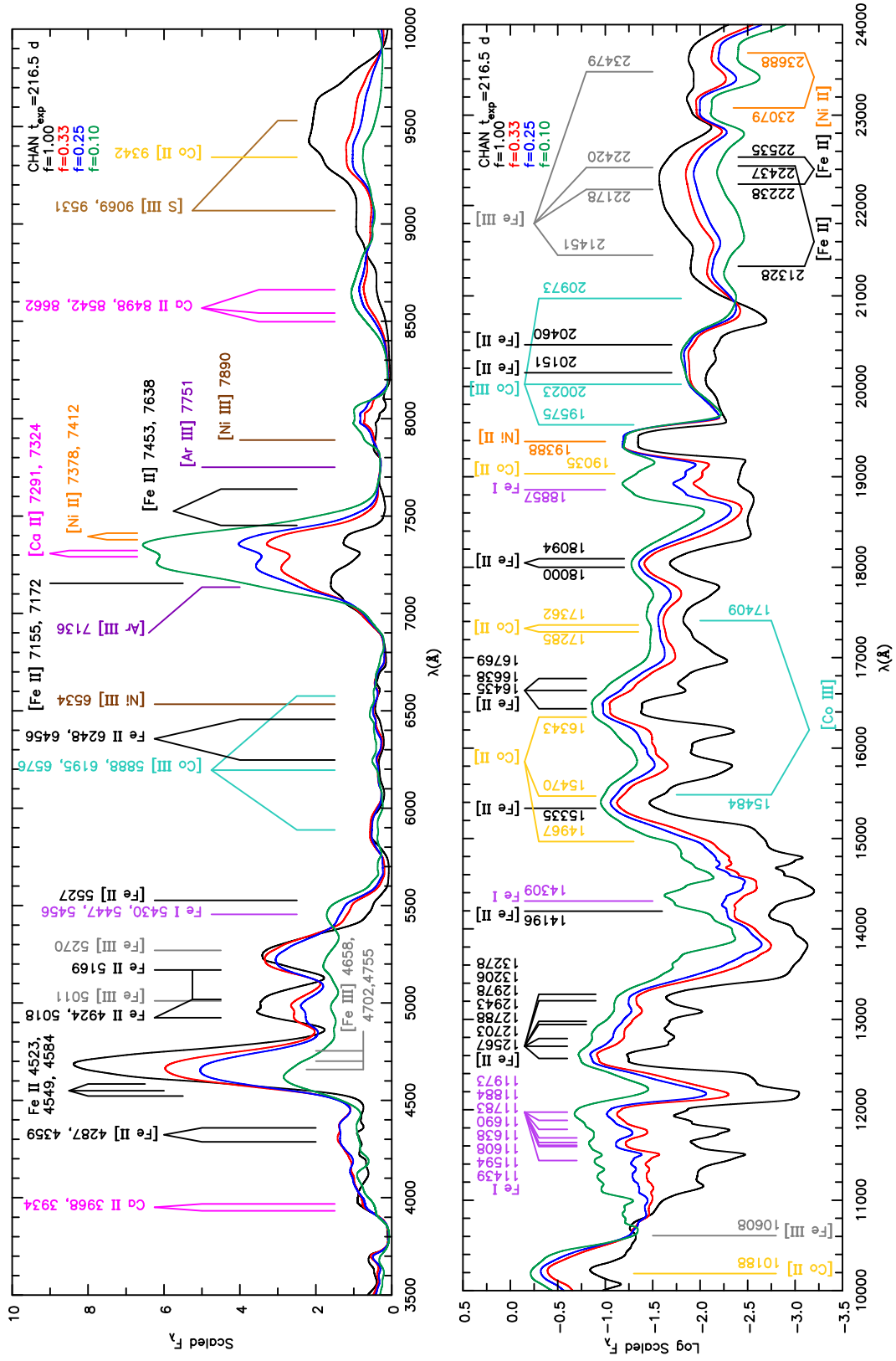

Figure 3. Spectra of CHAN at 216.5 d post-explosion compared to the spectra computed using different clumping factor values (0.33, 0.25, and 0.10). The spectra have all been scaled by the same value (and also to Fig. 2). To contrast the little flux in the NIR, we show the logarithm of the flux. Differences between the spectra can be large (greater than a factor of 10) for Fe I and Fe II features for just a factor of 3 or more in density.

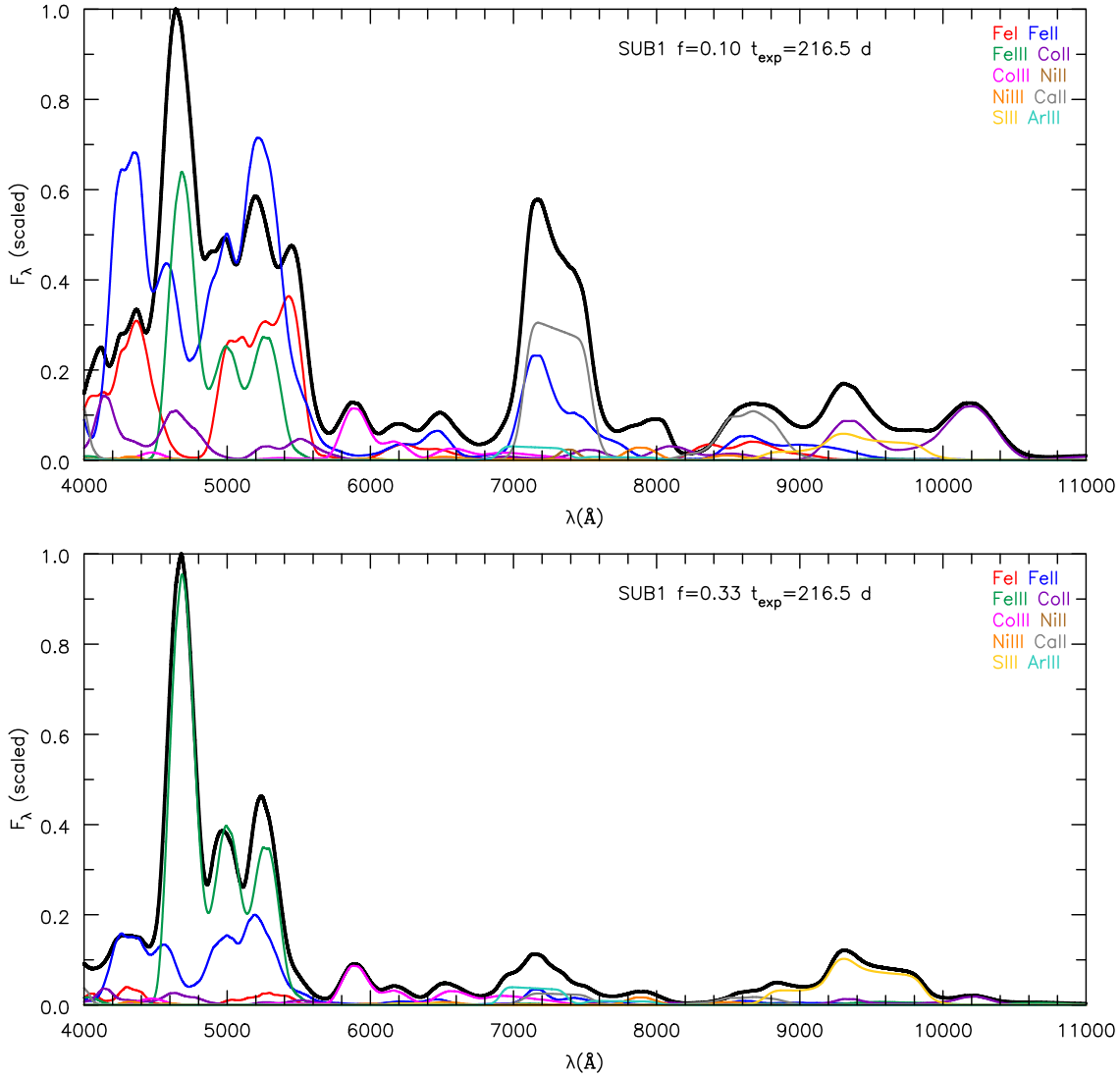

Figure 4. Observer's frame spectrum (thick black line) of SUB1 along with the component spectra of Fe I, Fe II, Fe III, Co II, Co III, Ni II, Ni III, Ca II, S III, and Ar III at 216.5 d post-explosion for a clumping factor of $f = 0.10$ and 0.33. If the optical depth effects are unimportant, the component spectrum will sum to the total to produce the full spectrum (thick black line). Conversely, we see that the features between 4000 and 5500 Å cannot be understood without allowing for optical depth effects. In model SUB1, there is no evidence for stable Ni emission near 7400 Å.

factor ($f = 1.00$, 0.33, 0.25, and 0.10). In order to contrast the little amount of flux in the NIR, we show $\log F_\lambda$ versus λ for wavelengths 1.0–2.4 μm. We also show the component spectrum for $f = 0.10$ and 0.33 for models SUB1 and CHAN, respectively, in Figs 4–7. These spectra will be discussed below.

3.1 Unclumped models

Before we discuss the influence of clumping, it is necessary to understand and summarize the results of Wilk et al. (2018), which do not incorporate clumping. This section focuses on two ejecta models, a direct detonation of a sub-$M_{\rm Ch}$ WD, and a DDT WD explosion model. Because our models come from two different explosion scenarios, the nucleosynthesis yields and stratification are model-dependent. 1D simulations of DDT explosions in $M_{\rm Ch}$ WDs produce what is known as a '^{56}Ni hole,' which is an underabundance of ^{56}Ni in the innermost region. This arises due to neutron-rich nuclear statistical equilibrium burning. Since our SUB1 model has lower central densities during explosion, it does not have a '^{56}Ni hole.' Therefore, SUB1 has a factor of about 2.26 less stable nickel. Within the '^{56}Ni hole' of CHAN, the temperature and ionization are lower than in the region containing the original ^{56}Ni.

Since stable nickel is centralized to the innermost part of the ejecta, it only becomes visible as the photosphere recedes inwards and the ejecta becomes optically thin. Hence, the ejecta transitions into the nebular phase. Thus, nebular spectra allow us to probe this once-shielded inner region. At 216 d post-explosion (roughly + 200 d post-maximum), we do not see in Figs 4 and 5 stable nickel in our SUB1 model, unlike in model CHAN. SUB1 has very little stable nickel in the inner region and also has Ni^{2+} as its dominant ionization (see fig. 7 of Wilk et al. 2018). At nebular times, we expect to see forbidden [Ni II] lines, particularly [Ni II] $\lambda\lambda$7378, 7412 and [Ni II] 1.939 µm, which are present in CHAN (see Fig. 3). In Figs 4–7, both models show strong emission from higher ionization states like Fe^{2+}, Co^{2+}, Ar^{2+}, and S^{2+}.

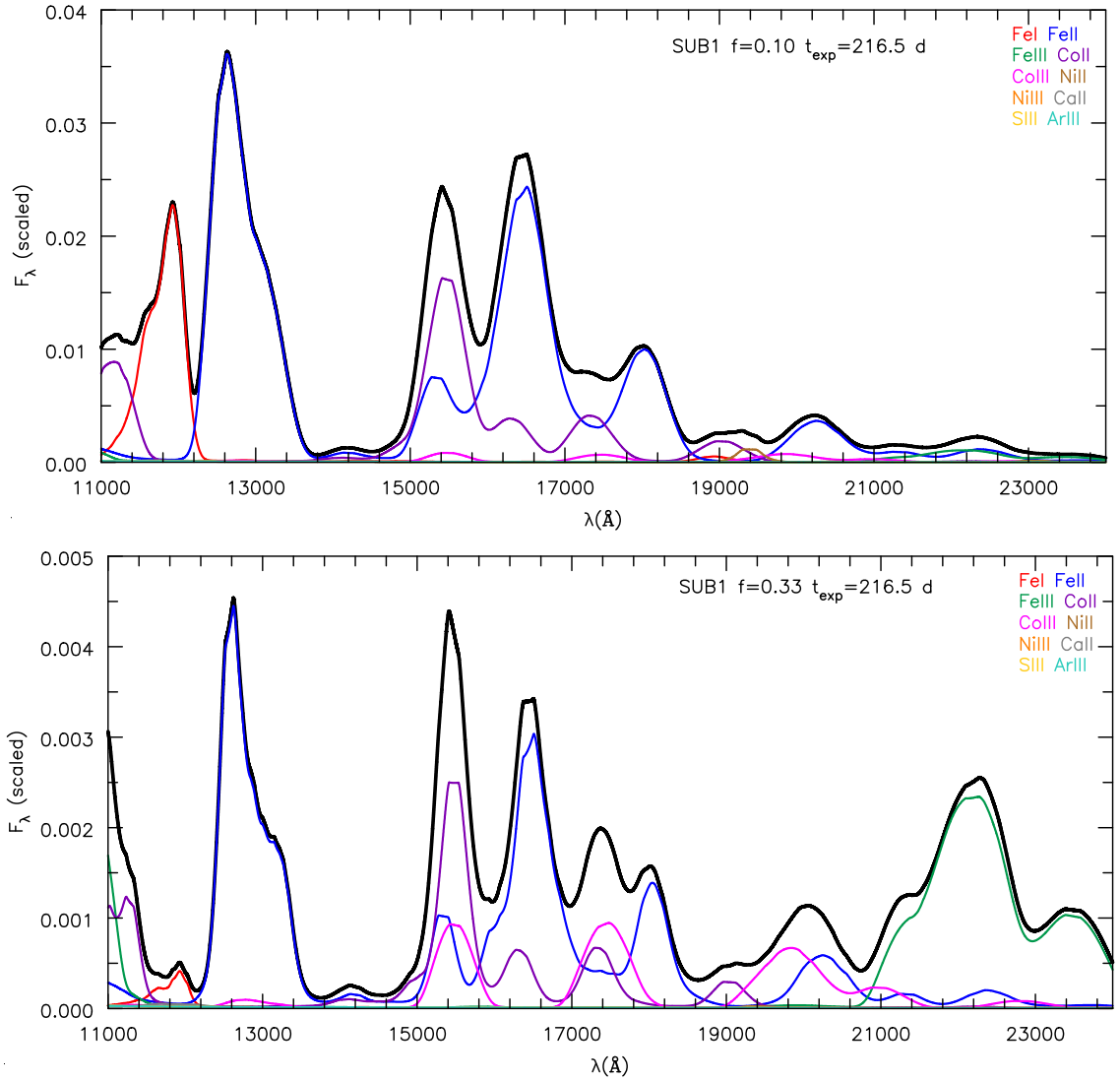

Figure 5. Observer's frame spectrum (thick black line) of SUB1 along with the component spectra of Fe I, Fe II, Fe III, Co II, Co III, Ni II, Ni III, Ca II, S III, and Ar III at 216.5 d post-explosion for a clumping factor of $f = 0.10$ and 0.33. If the optical depth effects are unimportant, the component spectrum will sum to the total to produce the full spectrum (thick black line). In model SUB1, there is no evidence for stable Ni emission near 19 400 Å.

At nebular times, the energy deposited by radioactive decay is equal to the energy radiated by numerous cooling lines. In the models, radioactive decay heats both the IGEs as well as the IMEs. However, it is necessary to determine if these ejecta models will still show spectral signatures of IMEs when clumping is introduced.

3.2 Ionization shifts

We show the average charge per species for sulphur, argon, calcium, iron, cobalt, and nickel for models with different amounts of clumping in Fig. 8. As expected, clumping shifts the ionization downwards in both models for the IGEs from mostly doubly ionized to singly ionized (i.e. $Fe^{2+} \rightarrow Fe^{+}$). The strength of Fe III, Co III, Ni III, S III, and Ar III lines decreases considerably with increasing clumping, while Fe II and Co II lines increase. For both SUB1 and CHAN, the average charge of sulphur, argon, and cobalt differs by almost one electron between $f = 1.00$ and 0.10 in the inner ejecta regions.

3.3 Impact on iron lines

Figs 2 and 3, as well as the component spectra in Figs 4–7, show that the Fe I, Fe II, and Fe III optical features depend strongly on the amount of clumping. The [Fe III] λλ4658, 4702 feature dropped in flux by more than a factor of 2 in both ejecta models from $f = 1.00$ to $f = 0.10$, while we saw the emergence of Fe I features between 4100 and 4500 Å and between 5400 and 5600 Å ($z\ ^5D^o_J - a\ ^5F_{J'}$ optical transitions). Figs 2–7 show the Fe I emission as a shoulder to the neighbouring [Fe III] and [Fe II] emission for $f = 0.33$ and 0.25, while we see a noticeable peak for $f = 0.10$.

While Fe II features were generally enhanced, the expected Fe II feature around 4359 Å (believed to be the $a^6S_{5/2}$–$a^6D_{7/2}$ transition and similarly the $a^6S_{5/2}$–$a^6D_{9/2}$ transition at 4287 Å) is weak or absent in our models compared with observations. An examination of the individual Fe I, Fe II, and Fe III spectra showed that the optical depth effects are important. It appears that the emergence of partially thick Fe I lines, Ti II lines like 4395 Å, and permitted Fe II lines reduce the strength of the claimed [Fe II] λλ4287, 4359 doublet believed to be seen in nebular spectra.

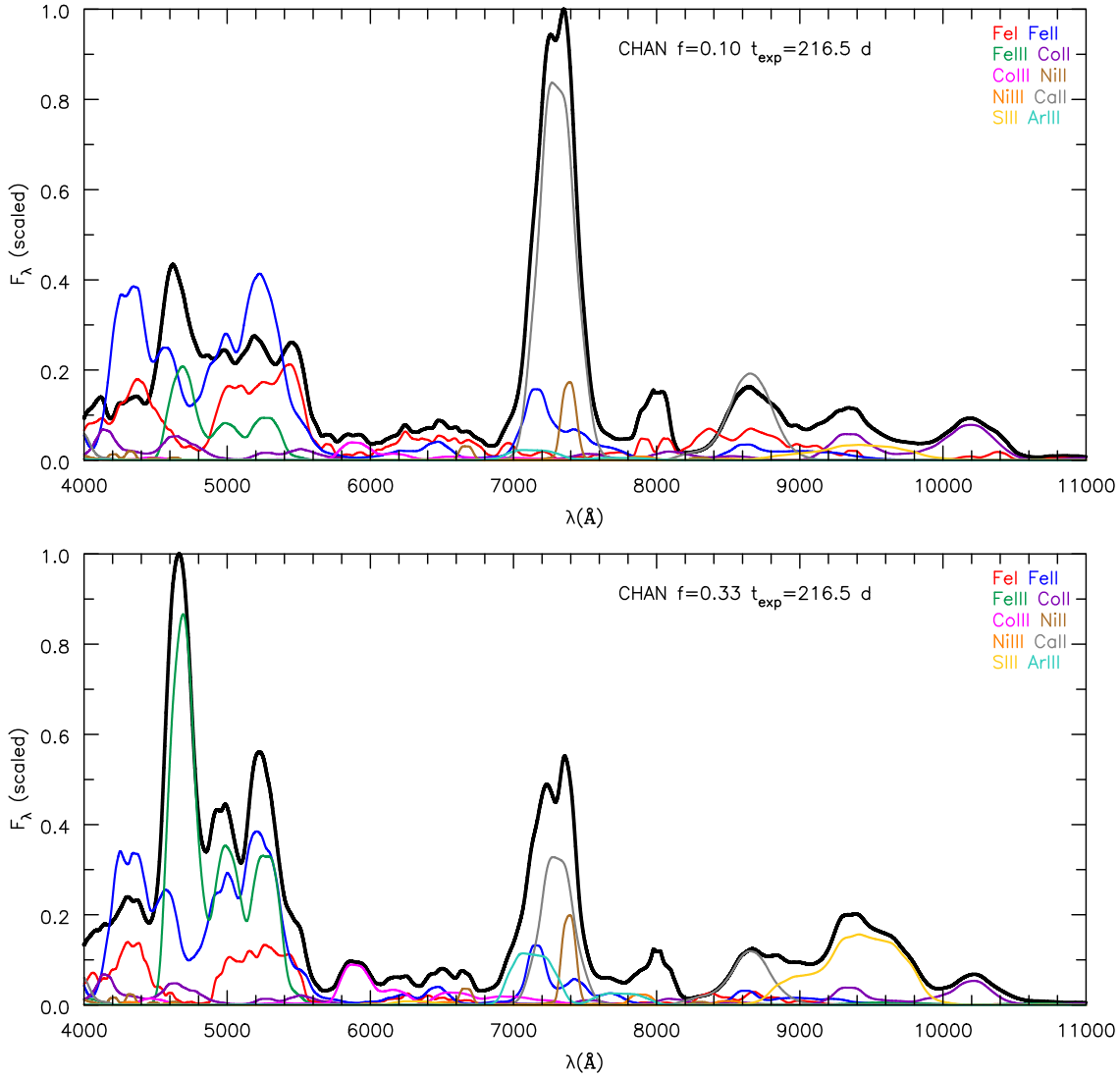

Figure 6. Observer's frame spectrum (thick black line) of CHAN along with the component spectra of Fe I, Fe II, Fe III, Co II, Co III, Ni II, Ni III, Ca II, S III, and Ar III at 216.5 d post-explosion for a clumping factor of $f = 0.10$ and 0.33. If the optical depth effects are unimportant, the component spectrum will sum to the total to produce the full spectrum (thick black line). Conversely, we see that the features between 4000 and 5500 Å cannot be understood without allowing for optical depth effects. In contrast with model SUB1, there is stable Ni emission near 7400 Å. As f decreases, emission in [S III] and [Ar III] weakens while that of [Ca II] increases.

In Figs 9 and 10, we show the optical depth to the [Fe II] λ4359 resonance zone (at velocity V) arising from interactions with other lines along the line of sight. There are tens of interacting lines to the outer ejecta and ∼25 000 interacting lines to the inner ejecta. Figs 9 and 10 show this optical depth (and the continuum optical depth) along a core ray through the ejecta. The line transitions with the largest optical depth contributions are Fe I] λ4384, Fe I] λ4375, Ti II λ4395, Fe II λ4385, and Fe I] λ4404. Differences between models and levels of clumping reflect the differences in the ionization of iron since the largest contributions to the optical depth primarily come from iron lines.

Studies of SN Ia nebular spectra often investigate the [Fe II] feature around 12 600 Å (Diamond et al. 2018; Maguire et al. 2018) since it is the least blended feature in nebular SN Ia spectra (free from other lines and ionization states of Fe). Our models confirm it is 'blend'-free. This line complex is therefore the best feature to constrain the Fe II-emitting region. We show in Fig. 11 that this [Fe II] feature can be reproduced by calculating an emission spectrum. To produce this emission spectrum, we use the temperature and ionization structure from CMFGEN and re-solve the level populations considering only collisional processes and radiative decays. The relativistic radiative transfer equation is then solved assuming zero opacity. We show this line complex can be inferred from tomography, as it is only sensitive to the temperature and ionization. However, this method will break down for departures from spherical symmetry.

Various observations of nebular SN Ia spectra show a slight shouldering on the 4600-Å iron complex due to a potential Fe I feature at 5500 Å – z $^5D^o_J$–a $^5F_{J'}$ optical transitions (Childress et al. 2015; Graham et al. 2017). Such Fe I features could constrain the level of ionization within SN ejecta and assist future modelling. Since Fe I features cause optical depth effects with [Fe II] λ4287, 4359, it is important to determine the Fe ionization. Despite all the observations showing [Fe II] λ4287, 4359, this feature has

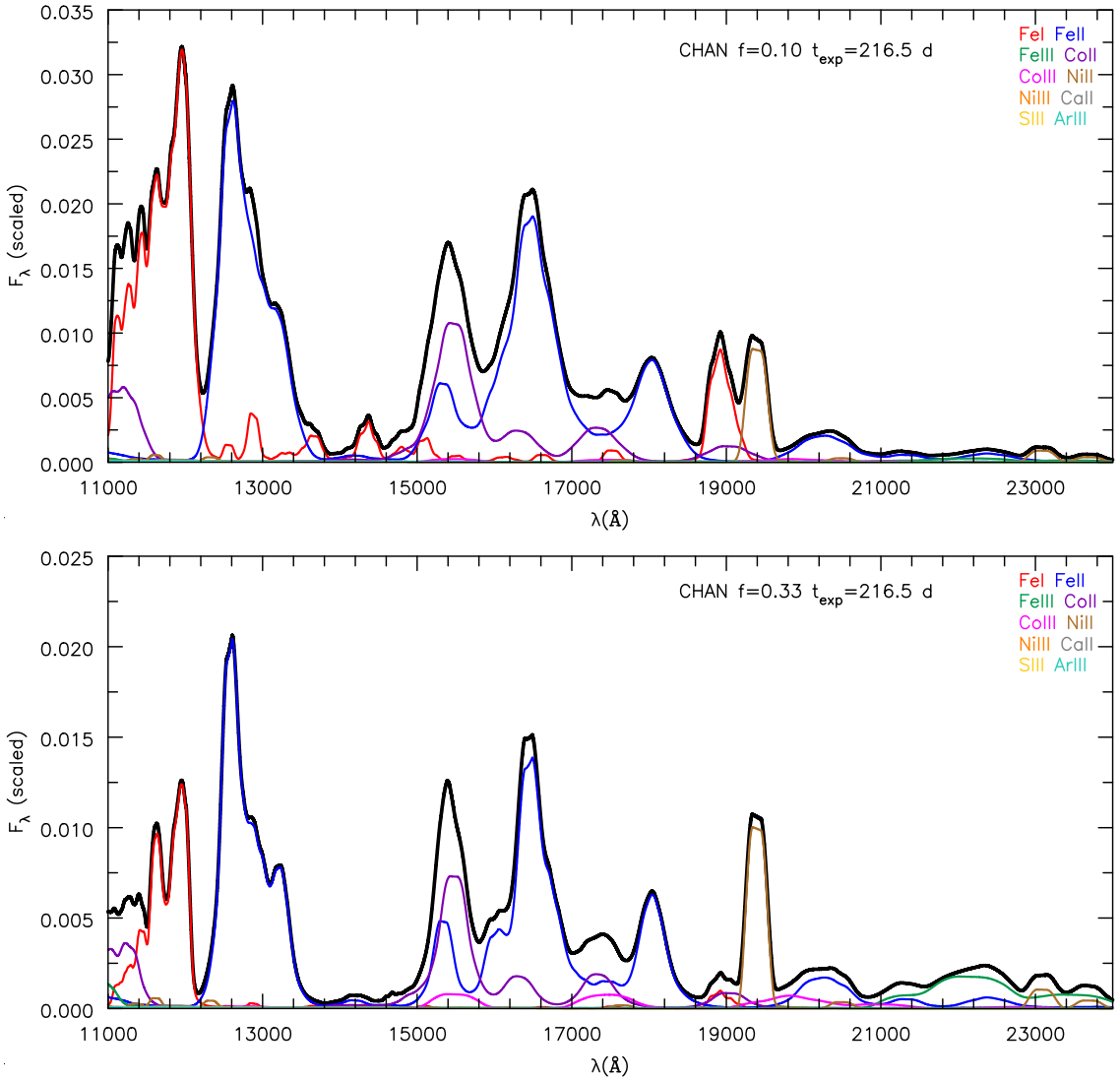

Figure 7. Observer's frame spectrum (thick black line) of CHAN along with the component spectra of Fe I, Fe II, Fe III, Co II, Co III, Ni II, Ni III, Ca II, S III, and Ar III at 216.5 d post-explosion for a clumping factor of $f = 0.1$ and 0.33. If the optical depth effects are unimportant, the component spectrum will sum to the total to produce the full spectrum (thick black line). In contrast with model SUB1, there is stable Ni emission near 19 400 Å.

yet to be accurately modelled by other researchers (Spyromilio, private communication; Sim, private communication). Shifts in the ionization of iron ($Fe^{2+} \rightarrow Fe^{+} \rightarrow Fe$) are expected as the ejecta continuously expands and cools as less energy is deposited from radioactive decays (Fransson & Jerkstrand 2015). Fransson & Jerkstrand (2015) showed that at very late times (1000 d), the 4600-Å iron complex, despite its similar appearance to early epochs, is dominated by emission from Fe I and Fe II.

3.4 [Ni II] 1.939 μm

In SUB1 models, the ionization fraction for nickel (Ni^{+}/ Ni^{2+}) drops in the inner region ($\lesssim$5000 km s^{-1}) by roughly three orders of magnitude when changing $f = 1.00$ to 0.10. However, the [Ni II] 1.939-μm line is still absent in SUB1. Where the line formation occurs, below ∼6500 km s^{-1}, the electron density is higher than 10^{7} cm^{-3} in the inner part of the ejecta, so its line emission scales linearly with density as we increase the amount of clumping. These densities are above the critical density for the upper level of this transition, so collisional de-excitations are important.

With $f = 0.10$ for SUB1, the weak [Ni II] 1.939- μm line is also a factor of a few weaker than [Co II] 1.9035 μm. SUB1 has more than a factor of 2 less stable nickel compared to CHAN (Table 1) in which we do still see the [Ni II] 1.939- μm line. With all of these factors such as ionization and abundance accounted for, it is not surprising that spectra of SUB1 still do not show this line.

3.5 Intermediate-mass elements

Due to the overlap in production/mixing of ^{56}Ni and IMEs in our models, the strength of IMEs is sensitive to the non-thermal heating and ionization structure within the ejecta. Within our models, a consequence of clumping is the enhancement of the [Ca II] λλ7291, 7324 doublet. The [Ca II] doublet is blended with the [Fe II] λλ7155, 7172, 7388 triplet and [Ar III] λ7136, and it contributes a large portion of the flux to the blended feature (see Figs 4–7). The [Ca II] emission flux is model-dependent. Not only is the mass

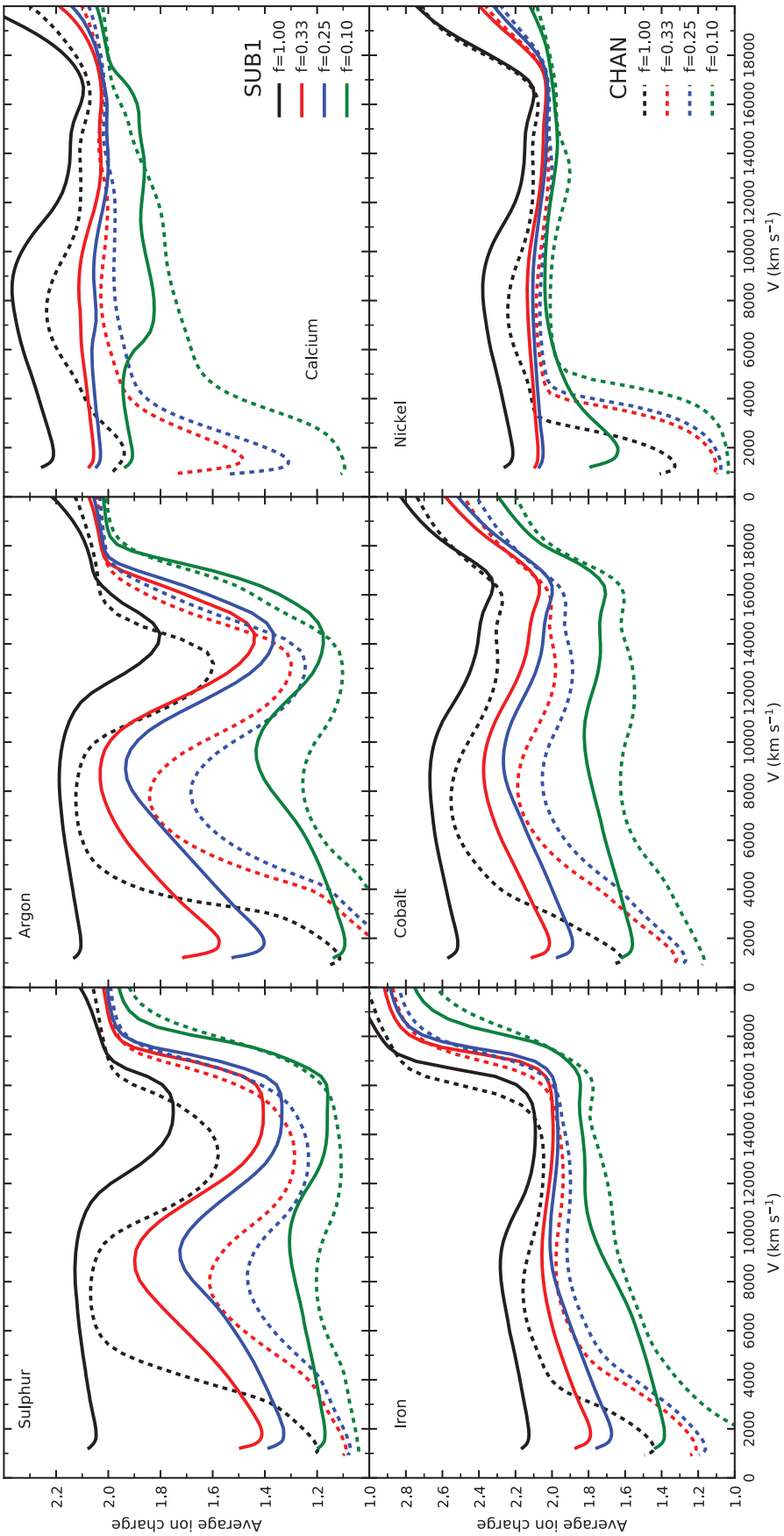

Figure 8. Average species charge for sulphur, argon, calcium, iron, cobalt, and nickel for models SUB1 and CHAN, and for clumping factors of 1.00, 0.33, 0.25, and 0.10 at roughly +200 d after maximum. For SUB1, the ionization is primarily sensitive to the clumping factor, and to the non-thermal energy deposited in the inner ejecta. Sulphur and argon show changes of roughly one electron, while iron shifts from mostly Fe^{2+} to nearly equal parts Fe^{2+} and Fe^{+}. The majority of the stable nickel is located in the inner ejecta, and in this region, the ionization is driven by the deposition of radioactive decay energy. These changes in the inner region give large changes in the predicted spectra. It is also apparent that relatively small changes in the clumping factor can give rise to large changes in the mean ionization level.

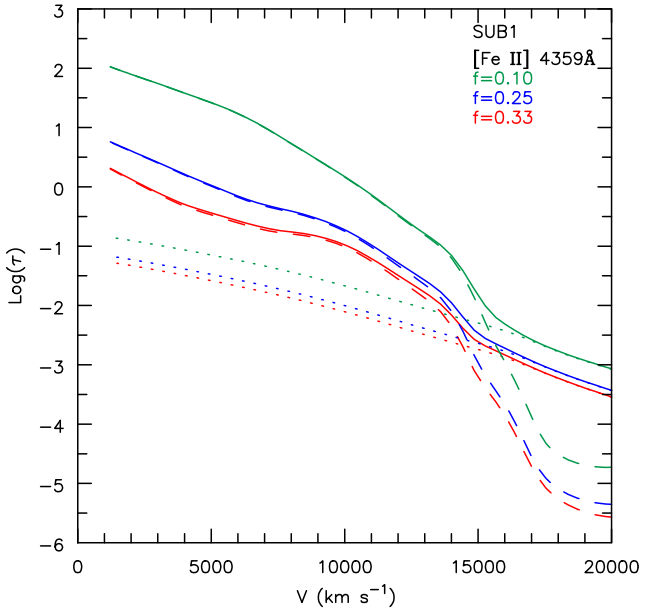

Figure 9. The optical depth to the [Fe II] λ4359 resonance zone at velocity V for various clumping factors for SUB1. We consider this along the first core impact parameter ($p_1 = 0$). The dashed lines correspond to the sum total of all lines that interact with the [Fe II] λ4359 line emitted at a particular resonance zone. The dotted lines correspond to the continuum contribution, and the solid lines represent the total [Fe II] λ4359 optical depth to the resonance zone.

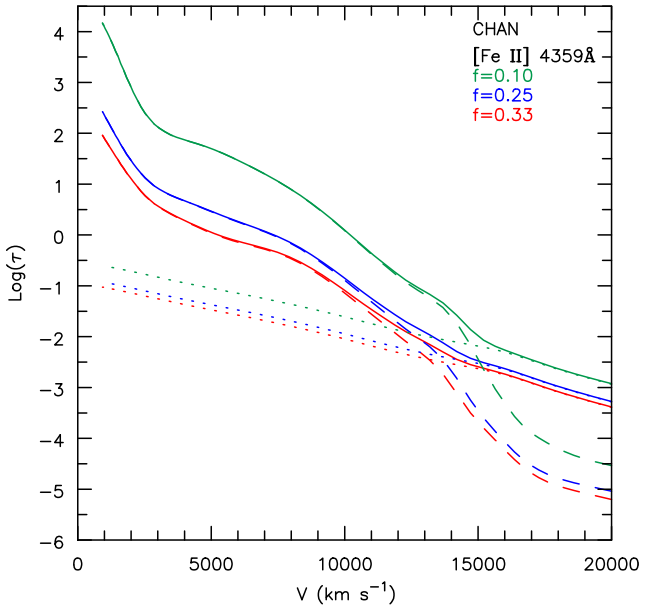

Figure 10. Same as Fig. 9 but now for model CHAN.

of calcium ∼1.75 times larger in CHAN than SUB1 but also the distribution of calcium varies significantly between SUB1 and CHAN. This is highlighted in Fig. 12, which shows the mass fractions of iron and calcium between the models as well as the cumulative distribution function of the energy deposition. In SUB1, the inner region containing 80 per cent of the energy deposited only contains 25 per cent of the calcium mass. In CHAN, however, the inner region containing 80 per cent of the energy deposited contains 50 per cent of the calcium mass. These models help constrain the amount of stratification between the original ^{56}Ni and IMEs required to produce SNe Ia nebular spectra.

Once the ionization is lowered, Ca^+ becomes the dominant cooling for the zone rich in IMEs, since S^+ and Ar^+, unlike their twice-ionized siblings, do not have strong cooling lines due to their low critical densities. We see the strength in the twice-ionized sulphur and argon lines ([S III] λλ9068, 9530 and [Ar III] λλ7135, 7751) decreases as we lower the clumping factor. However, it is unclear if such strong [Ca II] λλ7291, 7324 emission is seen in spectra of classic SNe Ia blended into the feature around 7200 Å, which is thought to be mostly [Fe II] and [Ni II], in nebular spectra (Taubenberger et al. 2013a; Bikmaev et al. 2015; Graham et al. 2017; Maguire et al. 2018). For low-luminosity 91bg-like SNe Ia (such as SN1999by), modelling suggests Ca emission is the dominant component of the 7200-Å feature at + 180 d (Blondin, Dessart & Hillier 2018).

If the 7200-Å feature is highly blended with [Ca II], then for a given electron density and temperature, we can predict an emissivity per ion ratio of the [Ca II] doublet to the [Fe II] lines using some simple physical assumptions. Assuming only collisional processes and radiative decays, we can solve for the atomic level populations for a range of temperatures and electron densities. Fig. 13 shows the emissivity ratio of the [Ca II] λ7291 transition to the [Fe II] λ7155 transition for a range of temperatures and electron densities with our simple assumptions. As shown in Fig. 13, for $N(Fe^+)/N(Ca^+) = 1$, the emissivity ratio between [Ca II] λ7291 and [Fe II] λ7155 for temperatures between 2000 and 7000 K to electron densities between 10^5 and 10^8 cm^{-3} is between a factor of 10 and 100. However, in our models, our $N(Fe^+)/N(Ca^+)$ is ∼5–30 between 5000 and 10 000 km s^{-1}. Therefore, we expect to see [Ca II] λλ7291, 7324 emission blended as long as the $N(Fe^+)/N(Ca^+)$ is $\lesssim$100. Although this only relates to the stronger component of the [Ca II] doublet, the [Ca II] λ7324 line comprises roughly 40 per cent of the overall contribution from [Ca II] (see Table 2). The other [Fe II]-blended components will contribute much less flux as the Einstein A values are a factor of 2 to 3 less than the [Fe II] λ7155 transition.

Despite the level excitation energy of Ca^+ $^2D_{5/2}$ and Fe^+ $a^2G_{9/2}$ being similar (∼16 per cent difference), the average-level populations in LTE can be several orders of magnitude different for the same total ion population. The average LTE-level population compared to the total is simply

$$\frac{\langle N(\mathrm{Fe}^+[\mathrm{a}^2\mathrm{G}_{9/2}])\rangle}{N(\mathrm{Fe}^+)} = \frac{1}{Z} g_{\mathrm{a}^2\mathrm{G}_{9/2}} \mathrm{e}^{-E[\mathrm{a}^2\mathrm{G}_{9/2}]/kT} = \frac{1}{Z} 10 \mathrm{e}^{-1.964\,\mathrm{eV}/kT}, \quad (1)$$

where Z is the partition function. For temperatures of 2000, 5000, and 10 000 K, the partition function (using the first 18 levels) is approximately 28, 43, and 58, respectively, assuming the states are in LTE with respect to the ground state. Since Fe^+ has many easily excited lower levels, it follows that even for the same Ca^+ and Fe^+ ion abundance, the emission from Ca II will dominate the blended feature at 7200 Å.

The strong emission of the [Ca II] λλ7291, 7324 doublet is not only a result of the ionization, temperature, and electron density but also coupled to the radiation field. The Ca II H&K lines have large oscillator strengths and can pump electrons into the upper $^2P^o$ levels. They then decay to the ^2D state, which again decays to the ^2S ground state, giving us [Ca II] λλ7291, 7324 emission. We have taken our ionization, temperature, and electron density

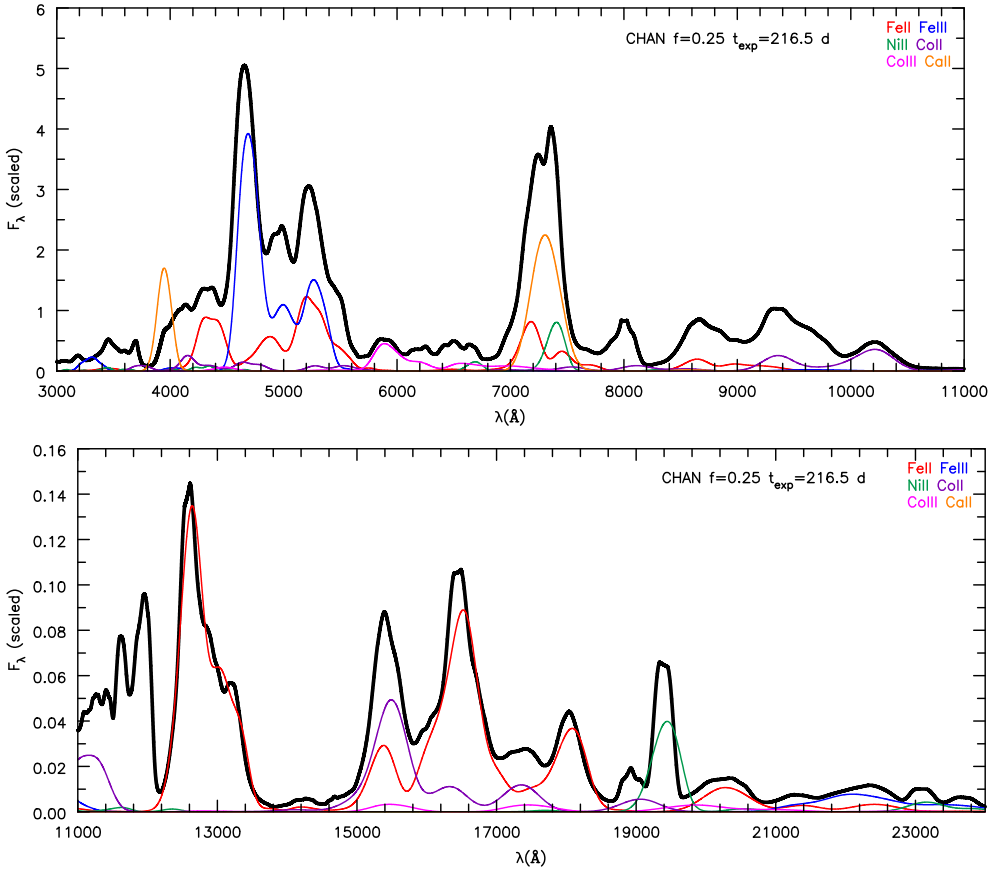

Figure 11. Observer's frame emission spectra of Fe II, Fe III, Ni II, Co II, Co III, and Ca II. We show the full observer's frame spectrum in black. The emission spectra are calculated by taking the temperature and ionization structure output from CMFGEN and re-solving the level populations assuming only collisional processes and radiative decays. We assume Gaussian emission profiles of 100 km s^{-1} in the co-moving frame.

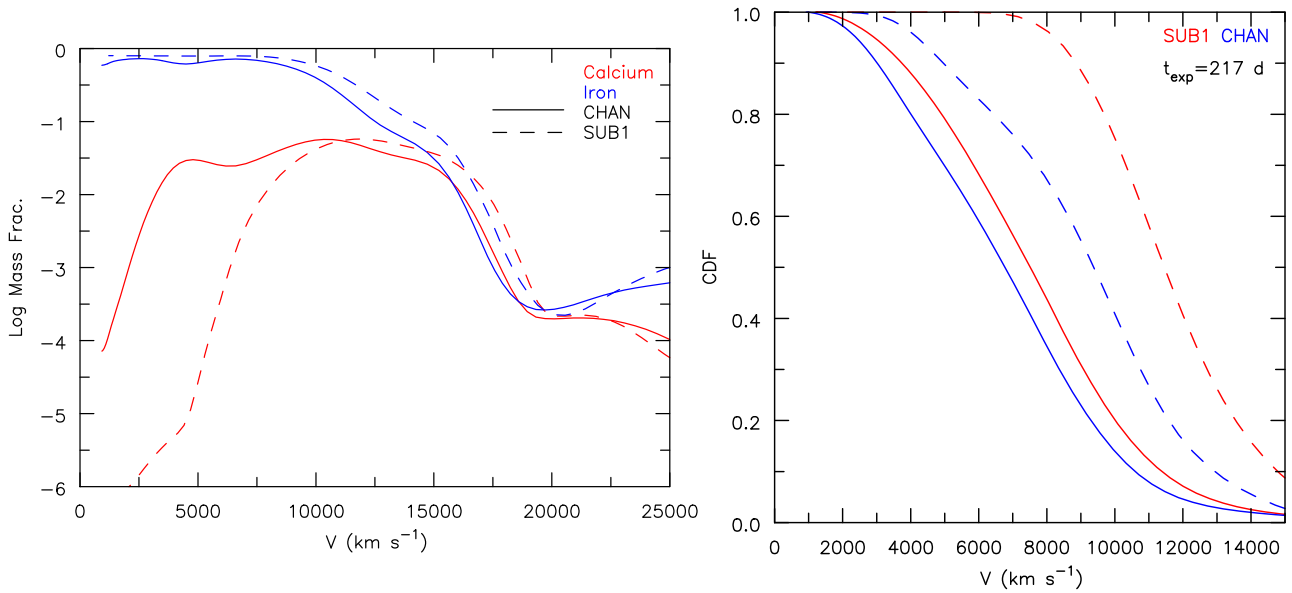

Figure 12. The left-hand panel shows the mass fractions for calcium and iron in both models. The solid line corresponds to model CHAN, and the dashed line corresponds to SUB1. The right-hand panel shows the cumulative distribution function for the energy deposition (solid lines) and the calcium mass (dashed lines) at 217 d after explosion (roughly + 200 d).

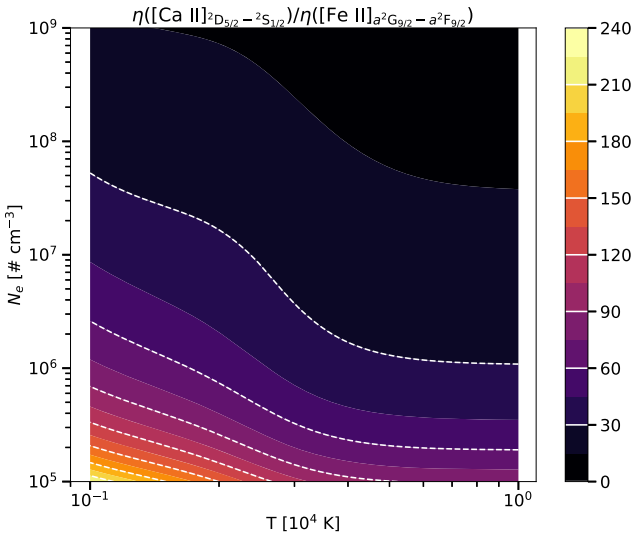

Figure 13. Line emission ratio of the [Ca II] λ7291 to [Fe II] λ7155 assuming N(Fe^+)/N(Ca^+) = 1. The emission ratio is calculated by solving the rate equations with only collisional and radiative decay terms for a fixed ionization of N(Fe^+)/N(Ca^+) = 1. The emission ratio favours strong calcium. When this ionization ratio is $\gtrsim$50, the iron would begin to dominate the 7200-Å complex.

structure from CMFGEN and re-solved for the level populations of Ca^+ assuming only collisional and radiative decay processes. For levels that are coupled to UV transitions, this assumption is only accurate within 50 per cent. We then solved the relativistic radiative transfer equation for line emission of Ca II with zero opacity. Our results (see Fig. 11) show that the spectra of Ca II is sensitive to the radiation field. Flux is absorbed in the Ca II H&K lines which can then be emitted in the Ca II NIR triplet as well as the [Ca II] λλ7291, 7324 doublet. Despite the critical densities for Ca^+ $^2D_{3/2}$ and $^2D_{5/2}$ being of the order of $\sim 10^5 - 10^6$ cm^{-3}, the atomic levels above the Ca^+ $^2D_{3/2}$ and $^2D_{5/2}$ have sufficiently high critical densities, which inhibit collisional de-excitations locking these levels to their LTE value.

Such strong [Ca II] emission could indicate a problem with our atomic data for Fe I/Fe II or likely be an indication of more stratified material in our 1D models. Element stratification within the ejecta also influences the strength of the lines belonging to IMEs. In particular, the presence of some ^{56}Co in the IME zone means that positrons are available as a heating source after the ejecta has become optically thin to γ-ray photons. However, even at late times, this contributes only a fraction of non-thermal heating in the inner region. γ-rays still scatter out into the ejecta, heating some of the outer layers.

If the problem lies not with our atomic data, then stratification is the cause of strong IME emission. This puts a constraint on the nucleosynthetic distribution of calcium produced in SNe Ia. This either prohibits an overlap between the calcium and the radioactive isotopes like ^{56}Ni, or this constrains the mass of calcium produced during the nucleosynthesis. Not surprisingly, when we artificially scale down the mass of calcium by a factor of 2 in our CHAN $f = 0.25$ clumped model, the peak flux drops by half. This also has implications for understanding early-time light curves. In order to produce the blue colours of SNe Ia, studies routinely mix ^{56}Ni into the outer layers of the ejecta in DDT models.

4 CONCLUSION

We have performed 1D radiative transfer calculations using CMFGEN for two ejecta models (one sub-M_{Ch} detonation and one M_{Ch} DDT with a stable iron core – see Wilk et al. 2018 for more details) utilizing micro-clumping at 216.5 d post explosion. Our goal was to understand the influence of micro-clumping on nebular spectra and to test when clumped models would provide a better fit to the observed level of ionization in Type Ia spectra. Clumping is expected to occur naturally in SN ejecta and this reduces the ionization by enhancing recombination. Because the luminosity comes from regions where energy is being deposited, it is crucial to reduce the ionization in these regions to match observed spectra. Even though the model CHAN has a stable iron core, its presence was not sufficient to stop the ionization from being higher than what is seen in observed spectra. We considered three different clumping factors, 0.33, 0.25, and 0.10, which we assumed were constant throughout the ejecta. Our models are in a regime where potentially small changes can shift the ionization. This also means that our models are sensitive to atomic physics.

Clumping lowers the average ionization of all species. The average ionization of IMEs is reduced by about one electron below 10 000 km s^{-1} and roughly by one half of an electron for IGEs (except cobalt which is reduced by roughly an electron). Despite clumping lowering the ionization in SUB1, the nickel ionization remained high in the inner region due to the lack of a '^{56}Ni hole.' With an already reduced stable nickel mass compared to CHAN, SUB1 failed to show strong emission from Ni II in the optical and in the NIR with the [Ni II] 1.939-μm line.

As iron is the most abundant species in the inner ejecta at 216 d, clumping had the most visible effect on the flux of [Fe III] features such as [Fe III] λλ4658, 4702. As the iron ionization is lowered, the flux in Fe II features increases, and permitted Fe I lines near 5500 Å emerge. These Fe I lines cause a shoulder to form on the [Fe II] and [Fe III] optical blend between 4200 and 5400 Å. Our attempts to model the [Fe II] λλ4287, 4359 feature were unsuccessful. While clumping generally enhanced the strength of [Fe II] features, absorption by other transitions limits its strength. Despite the difficulty in reproducing [Fe II] λλ4287, 4359, we show that the [Fe II] complex around 12 500 Å is completely reproduced under simple physics assumptions of collisional and radiative decays from a given ionization and temperature structure. In the IR, particularly from 10 000 to 11 800 Å, changes in the flux of Fe I lines by several orders of magnitude occur for a factor of a few change in density.

For the same ^{56}Ni mass, M_{Ch} explosions produce more IMEs compared to sub-M_{Ch} explosions. We have seen that only large clumping can sufficiently suppress emission from IMEs such as Ar III and S III. However, as we increase clumping, both models show an increase in the [Ca II] λλ7291, 7324, doublet which dominates over the [Fe II] λ7155 feature. Since the presence/absence of [Ca II] in this 7200-Å blend is still highly uncertain, we suggest that SN Ia ejecta require less mixing between the original ^{56}Ni and the calcium distribution. Another possibility is that the Ni and Ca are not microscopically mixed. In that case, non-thermal energy deposited in the Fe region would be radiated by Fe, while the energy deposited in the IME region would be radiated primarily by IMEs. In this case, the strength of the [Ca II] lines relative to [Fe II] would be set by the amount of heating in each region.

Despite arguments that mixing is required to reproduce early-time light curves, mixing between layers of IMEs and ^{56}Ni is inconsistent with what is observed at nebular times, since the emission reflects

Table 2. Atomic data for the [Ca II] λλ7291, 7324 doublet and the [Fe II] multiple near 7200 Å. The parentheses (#) correspond to $\times 10^{\#}$, and $T_4 = T/(10^4\ \mathrm{K})$.

Upper level (u)			Lower level (l)			A_{ul}	Wavelength	$N_{crit}(T_4 = 0.1)$	$N_{crit}(T_4 = 0.5)$	$N_{crit}(T_4 = 1.0)$
Term	g	E_u (eV)	Term	g	E_l (eV)	(s^{-1})	(Å)	(cm^{-3})	(cm^{-3})	(cm^{-3})
						Ca^+				
$^2D_{5/2}$	6	1.699932	$^2S_{1/2}$	2	0.000	8.025(−1)	7291.469	7.722(5)	1.717(6)	2.125(6)
$^2D_{3/2}$	4	1.692408	$^2S_{1/2}$	2	0.000	7.954(−1)	7323.888	6.070(5)	1.290(6)	1.645(6)
						Fe^+				
a $^2G_{9/2}$	10	1.96448603	a $^4F_{9/2}$	10	0.23217278	1.4950(−1)	7155.157	5.165(6)	9.130(6)	9.618(6)
a $^2G_{7/2}$	8	2.02954814	a $^4F_{7/2}$	10	0.30129857	5.6950(−2)	7172.004	2.415(6)	4.010(6)	4.207(6)
a $^2G_{7/2}$	8	2.02954814	a $^4F_{5/2}$	6	0.35186476	4.3450(−2)	7388.178	2.415(6)	4.010(6)	4.207(6)
a $^2G_{9/2}$	10	1.96448603	a $^4F_{7/2}$	10	0.30129857	4.8450(−2)	7452.538	5.165(6)	9.130(6)	9.618(6)

where most of the energy is deposited. The strength of time-dependent IME features in nebular spectra is a crucial diagnostic for understanding both progenitors and explosion properties of SNe Ia.

Better atomic data are also important for modelling of Fe I/Fe II/Fe III features in nebular spectra. Because the focus of this work is only on nebular phase modelling, further work is necessary to test the time-dependent effects for various levels of clumping during earlier phases. It would be helpful to perform full time-series calculations. Clumping should be fully explored to truly understand the nature of the progenitors of SNe Ia.

ACKNOWLEDGEMENTS

DJH acknowledges partial support from STScI theory grant HST-AR-14568.001-A, and DJH and KDW thank NASA for partial support through theory grant NNX14AB41G. This research has made use of the CfA Supernova Archive, which is funded in part by the National Science Foundation through grant AST 0907903.

REFERENCES

Basko M., 1994, ApJ, 425, 264
Bikmaev I. F., Chugai N. N., Sunyaev R. A., Churazov E. M., Khamitov I. M., Sakhibullin N. A., Galeev A., Akhmetkhanova A. E., 2015, Astron. Lett., 41, 785
Bildsten L., Hall D. M., 2001, ApJ, 549, L219
Black C. S., 2018, PhD thesis, Dartmouth College
Black C. S., Fesen R. A., Parrent J. T., 2016, MNRAS, 462, 649
Black C. S., Fesen R. A., Parrent J. T., 2019, MNRAS, 483, 1114
Blondin S. et al., 2012, AJ, 143, 126
Blondin S., Dessart L., Hillier D. J., Khokhlov A. M., 2013, MNRAS, 429, 2127
Blondin S., Dessart L., Hillier D. J., Khokhlov A. M., 2017, MNRAS, 470, 157
Blondin S., Dessart L., Hillier D. J., 2018, MNRAS, 474, 3931
Boffi F. R., Stanghellini L., 1994, A&A, 284, 248
Botyánszki J., Kasen D., 2017, ApJ, 845, 176
Bouret J. C., Lanz T., Hillier D. J., Heap S. R., Hubeny I., Lennon D. J., Smith L. J., Evans C. J., 2003, ApJ, 595, 1182
Bowers E. J. C., Meikle W. P. S., Geballe T. R., Walton N. A., Pinto P. A., Dhillon V. S., Howell S. B., Harrop-Allin M. K., 1997, MNRAS, 290, 663
Childress M. J. et al., 2015, MNRAS, 454, 3816
Chugai N. N., 1992, Sov. Astron. Lett., 18, 168
Dessart L., Hillier D. J., Wilk K. D., 2018, A&A, 619, A30
Diamond T. R. et al., 2018, ApJ, 861, 119
Dong S., Katz B., Kushnir D., Prieto J. L., 2015, MNRAS, 454, L61
Fink M., Hillebrandt W., Röpke F. K., 2007, AAP, 476, 1133
Fink M., Röpke F. K., Hillebrandt W., Seitenzahl I. R., Sim S. A., Kromer M., 2010, A&A, 514, A53
Fransson C., Jerkstrand A., 2015, ApJ, 814, L2
Gerardy C. L., 2002, PhD thesis, Dartmouth College
Gerardy C. L. et al., 2007, ApJ, 661, 995
Golombek I., Niemeyer J. C., 2005, A&A, 438, 611
Graham M. L. et al., 2017, MNRAS, 472, 3437
Hillier D. J., Miller D. L., 1999, ApJ, 519, 354
Houck J., Fransson C., 1992, AAS Meeting Abstracts, #76.03
Hoyle F., Fowler W. A., 1960, ApJ, 132, 565
Iwamoto K., Brachwitz F., Nomoto K., Kishimoto N., Umeda H., Hix W. R., Thielemann F.-K., 1999, ApJS, 125, 439
Kasen D., Röpke F. K., Woosley S. E., 2009, Nature, 460, 869
Khokhlov A. M., 1991a, A&A, 245, 114
Khokhlov A. M., 1991b, A&A, 245, L25
Kozma C., Fransson C., Hillebrandt W., Travaglio C., Sollerman J., Reinecke M., Röpke F. K., Spyromilio J., 2005, A&A, 437, 983
Leloudas G. et al., 2009, A&A, 505, 265
Leonard D. C., Li W., Filippenko A. V., Foley R. J., Chornock R., 2005, ApJ, 632, 450
Li H., McCray R., Sunyaev R. A., 1993, ApJ, 419, 824
Livne E., Arnett D., 1995, ApJ, 452, 62
Maeda K. et al., 2010a, Nature, 466, 82
Maeda K., Röpke F. K., Fink M., Hillebrandt W., Travaglio C., Thielemann F.-K., 2010b, ApJ, 712, 624
Maguire K. et al., 2018, MNRAS, 477, 3567
Maier A., Niemeyer J. C., 2006, A&A, 451, 207
Mazzali P. A., Hachinger S., 2012, MNRAS, 424, 2926
Mazzali P. A., Podsiadlowski P., 2006, MNRAS, 369, L19
Mazzali P. A., Cappellaro E., Danziger I. J., Turatto M., Benetti S., 1998, ApJ, 499, L49
Mazzali P. A., Maurer I., Stritzinger M., Taubenberger S., Benetti S., Hachinger S., 2011, MNRAS, 416, 881
Mazzali P. A. et al., 2015, MNRAS, 450, 2631
Mazzali P. A., Ashall C., Pian E., Stritzinger M. D., Gall C., Phillips M. M., Höflich P., Hsiao E., 2018, MNRAS, 476, 2905
Najarro F., 2001, Spectroscopy of P Cygni, Astronomical Society of the Pacific, California, United States, p. 133
Nomoto K., 1984, ApJ, 277, 791
Porter A. L. et al., 2016, ApJ, 828, 24
Puls J., Repolust T., Hoffmann T. L., Jokuthy A., Venero R. O. J., 2003, in van der Hucht K., Herrero A., César E., eds, Proc. IAU Symp. 212, A Massive Star Odyssey: From Main Sequence to Supernova. Kluwer, Dordrecht, p. 61
Ruiz N., Guerrero M. A., Chu Y.-H., Gruendl R. A., 2011, AJ, 142, 91
Ruiz-Lapuente P., Lucy L. B., Danziger I. J., 1992, Mem. Soc. Astron. Ital., 63, 233

Ruiz-Lapuente P., Kirshner R. P., Phillips M. M., Challis P. M., Schmidt B. P., Filippenko A. V., Wheeler J. C., 1995, ApJ, 439, 60
Seitenzahl I. R. et al., 2013, MNRAS, 429, 1156
Smareglia R., Mazzali P. A., 1997, in Hunt G., Payne H., eds, ASP Conf. Ser. Vol. 125, Astronomical Data Analysis Software and Systems VI. Astron. Soc. Pac. , San Francisco, p. 226
Srivastav S., Ninan J. P., Kumar B., Anupama G. C., Sahu D. K., Ojha D. K., Prabhu T. P., 2016, MNRAS, 457, 1000
Stasińska G., Gräfener G., Peña M., Hamann W. R., Koesterke L., Szczerba R., 2004, A&A, 413, 329
Stehle M., Mazzali P. A., Benetti S., Hillebrandt W., 2005, MNRAS, 360, 1231
Taubenberger S. et al., 2013a, MNRAS, 432, 3117
Taubenberger S., Kromer M., Pakmor R., Pignata G., Maeda K., Hachinger S., Leibundgut B., Hillebrandt W., 2013b, ApJ, 775, L43
Thomas R. C., Kasen D., Branch D., Baron E., 2002, ApJ, 567, 1037
Wang C.-Y., 2008, ApJ, 686, 337
Wilk K. D., Hillier D. J., Dessart L., 2018, MNRAS, 474, 3187
Woosley S. E., 1988, ApJ, 330, 218
Woosley S. E., 1997, ApJ, 476, 801
Woosley S. E., Weaver T. A., 1994, ApJ, 423, 371
Yaron O., Gal-Yam A., 2012, PASP, 124, 668

This paper has been typeset from a TEX/LATEX file prepared by the author.